Fabrication of air bridges on (100) β-Ga_2O_3 using crystallographic HCl gas etching

Cite as: AIP Advances 15, 055207 (2025); doi: 10.1063/5.0260753
Submitted: 26 January 2025 • Accepted: 7 April 2025 •
Published Online: 5 May 2025

Takayoshi Oshima[a] and Yuichi Oshima

AFFILIATIONS

Research Center for Electronic and Optical Materials, National Institute for Materials Science, Tsukuba, Ibaraki 305-0044, Japan

[a]Author to whom correspondence should be addressed: OSHIMA.Takayoshi@nims.go.jp

ABSTRACT

β-Ga_2O_3 air bridges on (100) substrates were fabricated through a self-aligning process that used conventional anisotropic BCl_3/Ar-plasma etching and crystallographic plasma-free HCl gas etching. The former etching can be done as vertical etching to expose the etched sidewalls, whereas the latter etching enables horizontal etching that is aligned with the (100) plane owing to the high etch resistance due to the lowest surface energy density of the (100) plane. By combining the two orthogonal etching techniques with other standard device fabrication processes, we were able to create air bridges. We believe that the undercut etching method demonstrated herein will facilitate the fabrication of micro-electromechanical systems.

In recent years, β-Ga_2O_3 has emerged as a promising ultra-wide bandgap semiconductor. As β-Ga_2O_3 has a bandgap of 4.43 eV,[1] its Baliga's figure of merit surpasses those of traditional wide bandgap materials such as SiC and GaN and makes it an excellent candidate for power device applications.[2] Because of its corresponding optical absorption edge at 280 nm, β-Ga_2O_3 exhibits native solar-blind sensitivity without bandgap tuning, making it a suitable material for solar-blind and flame detectors.[3,4] In addition, as β-Ga_2O_3 responses to reducing and oxidizing gases, it is applicable to gas sensors.[5,6] Furthermore, large β-Ga_2O_3 bulk single crystals with controlled conductivity can be grown with the use of melt growth techniques.[7–11] This makes it possible to produce low-cost, high-crystalline wafers and substrates for device fabrication. These advantages have driven the rapid progress in the research and development of β-Ga_2O_3-based devices and have led to the realization of high-performance devices.[12]

Along with its electrical, optical, and gas-sensing advantages, β-Ga_2O_3 is characterized by excellent mechanical properties, including a relatively high Young's modulus of ~261 GPa and an acoustic velocity of ~6623 m s^{-1}, which make it well-suited to micro-electromechanical systems (MEMS).[13] Through the integration of their electrical, optical, chemical sensing, and mechanical properties, β-Ga_2O_3 MEMS components are particularly valuable in high-power, high-frequency devices and resonance-enabled solar-blind ultraviolet photodetectors and gas sensors.[13] Recent advances in β-Ga_2O_3-based MEMS highlight the material potentials in high-frequency resonators,[14–16] vibrating channel transistors,[17] and resonant UV and gas sensors.[18–20]

To use MEMS devices in practical applications, one must create mechanically suspended and movable structures or air-gap structures. For superior MEMS performances, such structures are made of a single-crystalline and carrier-density-controlled epitaxial film grown on a native bulk substrate according to a methodology that is compatible with semiconductor device processes.[13] A heteroepitaxial film on a foreign substrate cannot substitute for the homoepitaxial layer due to its polycrystalline nature, which inevitably degrades the MEMS performances. Furthermore, direct fabrication of air-gap structures on β-Ga_2O_3 substrates eliminates the need for heterointegration or the exfoliation-transfer process, thereby simplifying the MEMS fabrication and reducing process costs. In addition, β-Ga_2O_3-based MEMS on β-Ga_2O_3 substrates can avoid undesired damage caused by the exfoliation process. However, no fabrication has been reported for air-gap structures directly on β-Ga_2O_3 substrates without the use of a transfer process. The aforementioned reported MEMS devices were fabricated by transferring β-Ga_2O_3 membranes and nanostructures onto prepatterned foreign

substrates;[15–20] however, the size and geometry were uncontrollable in this setting, which presents a significant challenge in practical applications.

We consider crystallographic etching, or facet-selecting etching, to be a viable undercut technique for fabricating air-gap structures. Several crystallographic etching techniques have been reported to date. In the case of wet etching techniques, such as hot phosphoric acid etching[21–23] and photoelectrochemical etching,[24,25] the (010) plane exhibits the highest etch resistance[22–24] due to its lower atomic and bond density.[24,25] By comparison, in the case of gas etching without plasma excitation, such as in HCl gas etching,[26–30] forming gas etching,[31] and hydrogen-environment anisotropic thermal etching,[32–34] the (100) plane exhibits the strongest etch resistance[26–29,31–34] due to the lowest surface energy density.[35] Furthermore, the high etch resistance of the (100) plane is a common feature in reduction etching with the use of Ga species, such as Ga-flux[36,37] and triethylgallium gas.[38,39] These anisotropic etching features have been used as a plasma-damage-free vertical etching technique for the fabrication of trenches and fins, whose etched sidewalls are created from high-etch-resistant planes.[23,28,29,31–34,37,39] These facts suggest that it is possible to create air-gap structures via horizontal undercutting of β-Ga_2O_3 crystals if the crystallographic etching technique and crystal orientation are appropriately selected. The possible choices are wet etching on the (010) plane or gas etching on the (100) plane. It should be noted that the (100) orientation is not commonly used in β-Ga_2O_3 power devices with epitaxial layers due to the formation of twinning during homoepitaxy.[40] However, twinning can be suppressed on miscut substrates,[41] enabling the demonstration of high-performance power devices.[42,43] Therefore, the (100)-orientation substrate could serve as a viable platform even for the aforementioned power MEMS applications. In this study, we conducted HCl gas etching experiments on (100)-oriented β-Ga_2O_3 substrates. After measuring the anisotropic horizontal etch rates, which were faster than the vertical etch rate in all in-plain directions, we fabricated air bridges using the strong horizontal etching feature.

We used (100) β-Ga_2O_3 single-crystal substrates cleaved from a bulk single crystal grown via an edge-defined film-fed growth method[8] (Novel Crystal Technology, Inc.). It is noteworthy that the primary cleavage plane of β-Ga_2O_3 is (100) because this plane has the lowest surface energy density,[35] thus cleaving is a facile process to obtain (100) substrates. Figure 1 shows the atomic arrangement projected in the surface normal direction, or the [201] direction. The two crystallographic symmetries of the monoclinic structure,[44] which have a mirror symmetry across the (010) plane, and a twofold rotational symmetry around the [010] axis can be seen in the atomic arrangement. Here, we focus on the vertically aligned low Miller index oxygen sublattice planes to understand the in-plane etching behavior because the fundamental crystal structure is constructed with O^{2-} ions, which have a larger radius than Ga^{3+} ions do. They are the (010), ($\bar{1}02$), ($\bar{1}\bar{1}2$), and ($\bar{1}12$) planes, as indicated in Fig. 1, and the corresponding in-plane directions are along the [001], [010], [021], and [02$\bar{1}$] directions, respectively. The side-etch characteristics related to these planes will be discussed later.

The etching experiments were carried out using various semiconductor device processes in conjunction with HCl gas etching. The SiO_2 layer was deposited at 350 °C by using plasma-enhanced chemical vapor deposition with tetraethyl orthosilicate and O_2 as

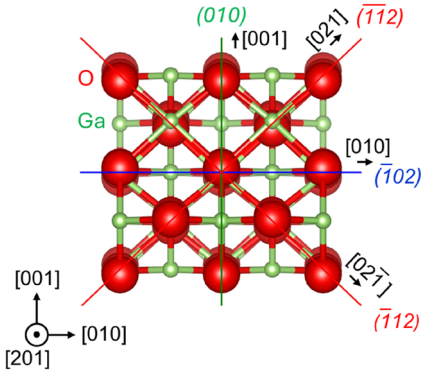

FIG. 1. (*Single column*) Atomic arrangement of the β-Ga_2O_3 structure projected along the [201] direction normal to the (100) plane. Low Miller index, oxygen sublattice planes vertical to the (100) plane, and the corresponding in-plane directions are also indicated.

the Si and O precursors, respectively. On the SiO_2 layer, a patterned photoresist mask was formed using optical lithography with a 375 nm focused laser. The SiO_2 layer was dry-etched without additional heating by CHF_3/N_2 capacitively coupled plasma (CCP) according to our standard process recipe (CHF_3 and N_2 flow rates of 25 and 25 sccm, respectively; chamber pressure, 3.0 Pa; and CCP power, 100 W). The standard etch rate for the SiO_2 was 0.028 μm min^{-1}. Note that β-Ga_2O_3 worked as an etch stopper for the CHF_3-based dry etching. The β-Ga_2O_3 substrate and, in some cases, the SiO_2 layer were dry-etched by BCl_3/Ar inductivity coupled plasma (ICP) with backside He cooling according to our standard process recipe (BCl_3 and Ar flow rates of 50 and 10 sccm, respectively; chamber pressure, 1.0 Pa; and ICP and bias powers of 500 and 30 W, respectively). The standard etch rates for β-Ga_2O_3 and SiO_2 were 0.12 and 0.053 μm min^{-1}, respectively, which means that the etch selectivity was ~2. The sample surface after the BCl_3/Ar-plasma etching was cleaned by immersing the sample in HNO_3 acid. The removal of the photoresist was done using oxygen plasma ashing and organic solvents. The crystallographic gas etching of the β-Ga_2O_3 substrate with a patterned SiO_2 mask was performed using a laboratory-made halide vapor-phase etching system in a gas flow having a mixture of HCl (>99.999% pure) and N_2 (dew point < −110 °C), where the HCl partial pressure was 62.5 Pa at 1038 °C under atmospheric pressure. The HCl partial pressure and process

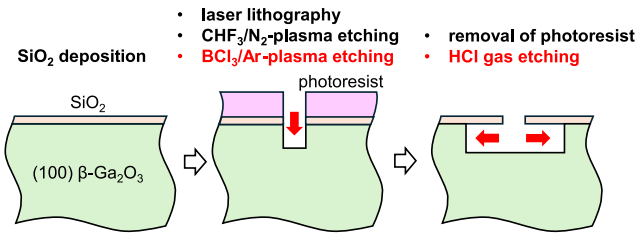

FIG. 2. (*Two columns*) Process flow for the horizontal etching on the substrate with (100) orientation.

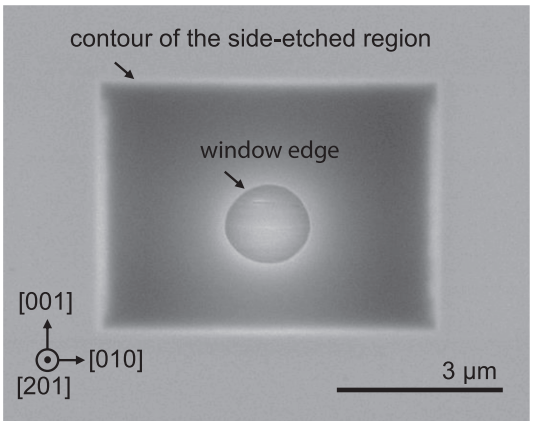

FIG. 3. (*Single column*) Plain-view scanning electron microscopy image of the HCl gas-etched structure created under a circular window. The acceleration voltage was set to 5 kV so that the side-etched region under the SiO_2 mask could be observed.

temperature were the same as those used in our previous experiments on the (001), (010), ($\bar{1}$02), and (011) substrates[26,28–30] The SiO_2 mask was removed with the use of buffered hydrofluoric acid.

The etched structures were observed using scanning electron microscopy (SEM). Cross sections were exposed along with the ($\bar{1}$02) plane, and they were recorded using focused ion beam (FIB)-SEM. Prior to the FIB milling, carbon was deposited on the local area to protect its surface structure. The thickness of the SiO_2 layer was measured using spectroscopic ellipsometry. The etching depth of the β-Ga_2O_3 substrate was measured using one of an ellipsometer, a stylus profiler, or the FIB-SEM system.

We first investigated the fundamental HCl gas etching characteristics on the (100) plane, with a particular focus on the in-plane anisotropy of the side etching. Given the high etch resistance of the (100) plane for HCl gas etching, BCl_3/Ar-plasma dry etching was employed as the vertical etching method for exposing the etched sidewalls in preparation for the subsequent HCl gas etching. Figure 2 shows our procedure. A (100) substrate covered with a 0.10 μm thick SiO_2 layer was etched using sequential CHF_3/N_2-plasma dry etching for 5 min and BCl_3/Ar-plasma dry etching for 9 min using a photoresist mask patterned by laser lithography. After dry etching, the remaining photoresist was removed, and the etched surface was cleaned using HNO_3. The window shapes were rectangular, and circular, and three types of wagon-wheel. The dimensions of the rectangular window were 100 × 150 μm. The diameter of the circular window was 1.50 μm. The two types of wagon wheels had 18 line-shaped windows, starting from [010] and [001] directions, respectively, with a width of 0.65 μm in 20° increments. The other type of wagon-wheel had 8 line-shaped windows positioned along the directions parallel to the vertically aligned oxygen sublattice planes (Fig. 1), with the same width as that of the other types. The

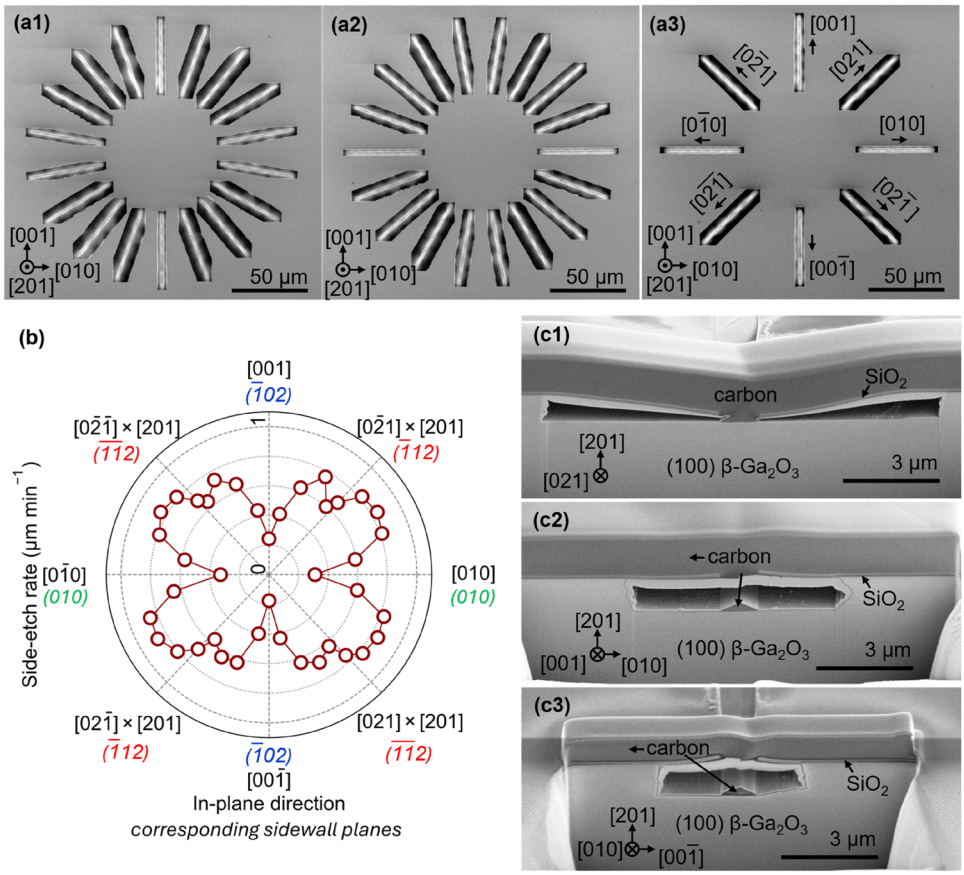

FIG. 4. (*Two columns*) Summary of scanning electron microscopy (SEM) observations of the HCl gas-etched trenches created under the wagon-wheel windows. Panels (a1)–(a3) show the plain-view SEM images for the three types of wagon wheels observed at an acceleration voltage of 5 kV. In panels (a1) and (a2), 18 line-shaped windows are arranged at 20° intervals, starting from the [001] and [010] directions, respectively. In panel (a3), the line-shaped windows are placed along the specific directions parallel to the vertically aligned oxygen sublattice planes (Fig. 1). (b) Polar plot of the side-etch rates perpendicular to the window lines extracted from panels (a1)–(a3). Panels (c1)–(c3) are 54° tilted-view cross-sectional SEM images of the etched trenches under the line-shaped windows aligned in the [021], [001], and [010] directions shown in panel (a3). In panels (c1)–(c3), the observed carbon deposits serve as protective layers for the focused ion beam milling process.

dry-etched depth of the β-Ga_2O_3 was 0.90 μm, which was measured using the step height at the rectangular window. For the dry-etched sample, HCl gas etching was carried out for 10 min.

The anisotropic etching behavior of the etched structures created under the windows was examined. The vertical etch rate was extracted and found to be ~0.03 μm min^{-1} by measuring the step heights at the boundary of the mask and the etched depression in the rectangular window. In contrast, the anisotropic side etching was visualized by SEM observation of the etched depression formed under the circular window, as shown in Fig. 3. The contour of the side-etched region was nearly rectangular, and its long and short etched sidewalls were parallel to the [010] and [001] directions, respectively, which indicates that the side-etch rates in the [001], [00$\bar{1}$], and ⟨010⟩ directions were relatively small. The side-etched shapes could be compared to elongated hexagons on the (001) and ($\bar{1}$02) planes[26,29] and a parallelogram on the (010) plane.[28] Furthermore, the etched trenches created under the wagon-wheel windows [Figs. 4(a1)–4(a3)] were investigated to obtain more information about the in-plane angular dependence of the side-etch rate. By measuring the side-etched lengths on both sides of the line-shaped windows, the side-etch rates were obtained and summarized in the form of polar coordinates, as shown in Fig. 4(b). The obtained plot pattern reflects the crystal symmetry. The [010] side pattern (right half) is almost equivalent to the [0$\bar{1}$0] side pattern (left half) due to their mirror symmetry, whereas the [001] side pattern (the top half) is somewhat different from the [00$\bar{1}$] side pattern (the bottom half) due to their twofold rotational symmetry. The side-etch rate was suppressed not only in the [001], [00$\bar{1}$], and ⟨010⟩ directions but also in the near directions perpendicular to [021] and [02$\bar{1}$]. The slower rates of the side-etch directions correspond to the vertically aligned oxygen lattice planes of ($\bar{1}$02), (010), ($\bar{1}$12), and ($\bar{1}\bar{1}$2), as illustrated in Fig. 1. It is noteworthy that the counters of the side-etched regions for the slower side-etch directions were relatively smooth relative to those of the other directions [compare Figs. 4(a1) and 4(a2) with Fig. 4(a3)]. Hence, the in-plane window directions of the [001], [010], [021], and [02$\bar{1}$] directions are important to the crystallographic etching on the (100) plane. The cross sections of the trenches along the [001], [010], and [021] directions in the wagon-wheel pattern were also observed [Figs. 4(c1)–4(c3)]. Note that information about the [02$\bar{1}$] trench could be estimated from that about the [021] trench, owing to their mirror symmetry. The etched bottom planes were flat, even under the masked regions, except for the [00$\bar{1}$] side-etched region in the [010] trench. The presence of a slope structure in the [00$\bar{1}$] side region is consistent with our previous experiment on the ($\bar{1}$02) substrate, in which HCl gas-etched [010] trenches exhibited (100)-like tapered sidewalls.[29] The uneven side-etching features in the [010] trench were not suitable for horizontal etching. Therefore, the window direction should be either [001], [021], or [02$\bar{1}$]. To evenly match the etch rates on the left and right sides, the window direction should be [001]. Although the side-etch rate was relatively slow in the ⟨010⟩ directions of the [001] trench, the ratio of the horizontal etch rate to the vertical etch rate was still as high as ~10.

We then fabricated β-Ga_2O_3-based air bridges on the (100) substrate. Figure 5 shows the procedural steps. The process involves repeating the vertical BCl_3/Ar dry etching and horizontal HCl gas etching twice. The first round of etching defined the width and height of the bridge, and the second round of etching undercut the crystal under the bridge. The bridge direction was set to [001] so that the amounts of undercut etching from both sides of the bridge were equal, as discussed in the previous paragraph. The length of the bridge in the CAD pattern for the laser lithography was set to 10.00 μm, whereas the widths of the bridge were set to 4.00 and 6.00 μm. The narrow-width and wide-width designs were intended for the fabrication of the air bridge and the bridge-like mesa (a mesa with unconnected undercut trenches on both sides), respectively. The details of the procedural steps are described along with the experimental results in the following paragraphs.

A SiO_2 layer having a thickness of 0.89 μm was deposited on a (100) β-Ga_2O_3 substrate and patterned to create a mask by laser lithography and anisotropic dry etching using CHF_3/N_2 gas plasma for 38 min, which was followed by the removal of the

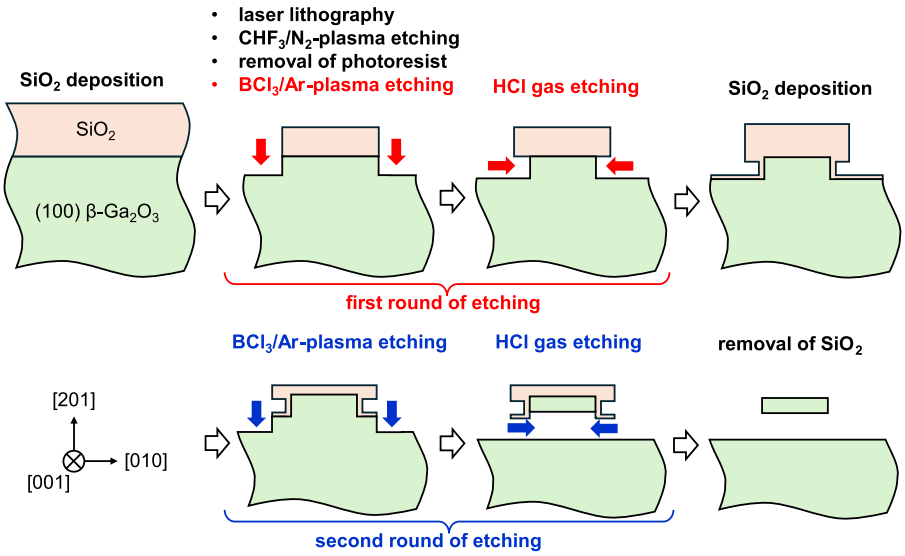

FIG. 5. (*Two columns*) Process flow for the β-Ga_2O_3-based air bridges along the [001] direction on the (100) orientation substrate.

photoresist. The first-round etching process began with dry etching by BCl_3/Ar gas plasma via the SiO_2 mask for 7 min, which was followed by a surface cleaning process in HNO_3. During the dry etching, β-Ga_2O_3 was etched to a depth of 0.81 μm to expose the sidewall surface, which had the same height as the etched depth, and the thickness of the remaining SiO_2 mask was decreased to 0.52 μm. The resulting bridge-shaped mesa structures exhibited lengths and widths of ~11.3 and ~4.6 μm, respectively, for the wide-width structure, and of ~11.3 and ~2.5 μm, respectively, for the narrow-width structure. Subsequently, the exposed sidewalls were slightly side-etched for 1.5 min using HCl gas etching. Taking a side-etch rate of 0.31 μm min^{-1} in the ⟨010⟩ directions into account, the expected side-etching length of both sidewalls was ~0.5 μm. Figures. 6(a1) and 6(b1) show the resulting structures.

After the first round of etching, the sample surface was coated with a layer of SiO_2 having a thickness of 0.12 μm. The deposited SiO_2 layer on the etched sidewalls worked as a mask layer for the second round of HCl gas etching, which was performed later. The thickness of the SiO_2 mask on the top surface of the bridge-shaped mesa was increased to 0.64 μm.

In the second round of etching, the β-Ga_2O_3 and SiO_2 were vertically etched simultaneously for 7 min using BCl_3/Ar plasma. In the region of the mask window, the thin SiO_2 layer was completely removed, and the underlying β-Ga_2O_3 crystal was further etched by 0.50 μm, thereby exposing the second sidewalls for the subsequent undercut etching. In the mask region, the SiO_2 layer was also etched but retained a thickness of 0.27 μm. After the dry etching, the sample was cleaned with HNO_3. Then, the undercut etching was performed by HCl gas etching for 8 min, which was designed to fully undercut the narrow-width bridge-shaped mesa. The calculated horizontal etch lengths were 2.5 μm. Figures. 6(a2) and 6(b2) show the resulting structures.

After the second round of etching, the remaining SiO_2 mask was removed. For the narrow-width structure, an air gap could be clearly observed, which indicates the fabrication of an air bridge [Fig. 6(a3)]. In the case of the wide-width structure, the surface SEM observation alone could not determine whether the ends of the undercut trenches were connected or unconnected [Fig. 6(b3)].

The narrow-width and wide-width structures were identified as the air bridge and the bridge-like mesa, as evidenced by the cross-sectional SEM observations shown in Figs. 7(a) and 7(b), respectively. The thickness and width of the air bridge were ~0.31 and ~1.2 μm, respectively [Fig. 7(a)]. The etched bottom surface of the bridge appeared to be relatively smooth. However, the surface morphology on the reverse side of the bridge was difficult to observe. This morphology was assumed to be smooth as well, because the bottom and reverse side planes were crystallographically equivalent. It should be noted that more of the crystal on the reverse side surface was etched than on the bottom surface. The reason for the strong

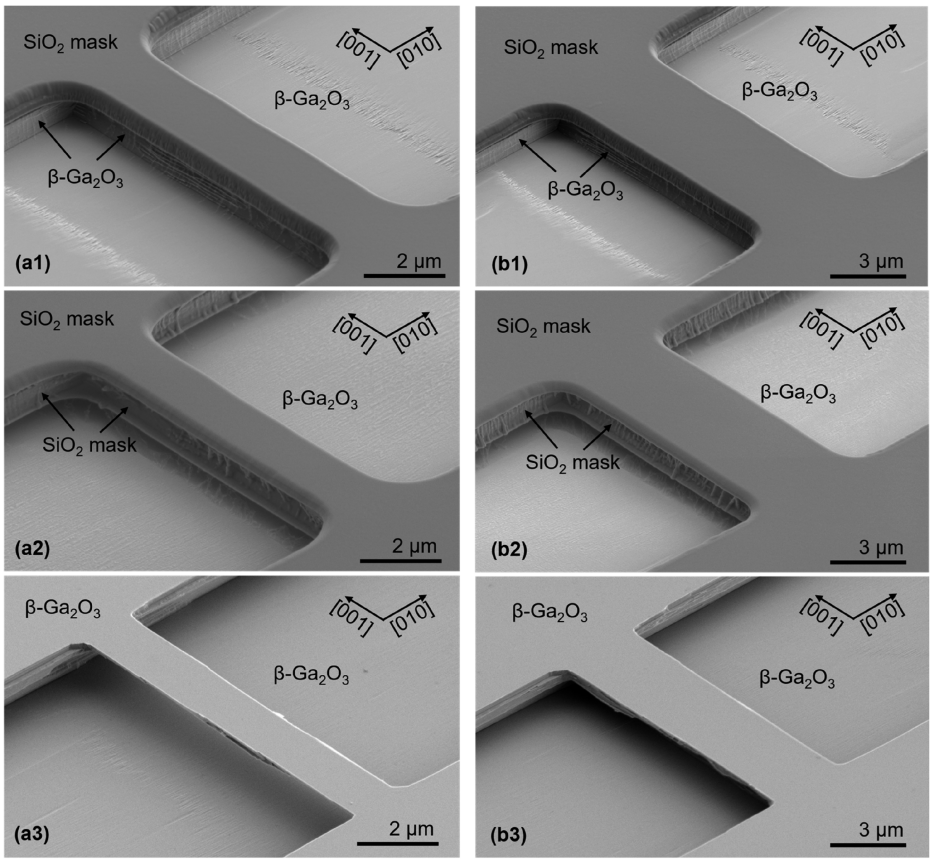

FIG. 6. (*Two columns*) Scanning electron microscopy images of the etched structures of (a1)–(a3) narrow and (b1)–(b3) wide widths. The images were recorded after (a1) and (b1) the first round of etching, after (a2) and (b2) the second round of etching, and after (a3) and (b3) the removal of the SiO_2 mask. Panels (a3) and (b3) show the air bridge and the bridge-like mesa structures, respectively.

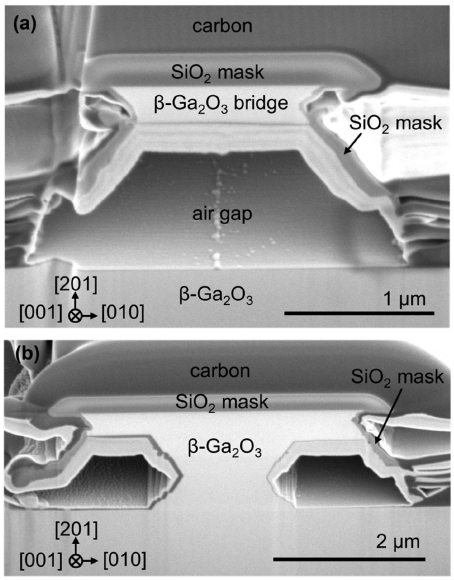

FIG. 7. (*Single column*) Cross-sectional scanning electron microscopy images of (a) the air bridge and (b) the bridge-like mesa structure with the SiO_2 mask, captured after the second round of etching. Note that panels (a) and (b) correspond to the structures shown in Figs. 6(a2) and 6(b2), respectively. The electron beam incidence was tilted at 54° with respect to the surface normal. The observed carbon deposit serves as a protective layer for the focused ion beam milling.

etching on the backside is unclear at the moment, but it should be clarified to improve the controllability of the etching process. Both ends of the horizontal trenches from the bridge-like mesa structure were found to be wedge-shaped [Fig. 7(b)]. These particular end structures are consistent with our previous HCl gas etching results on the (010) substrate, where the bottom ends of the vertical trenches were wedge-shaped and constructed with (310) and $(\bar{3}10)$ facets.[28] Wedge-shaped end structures were also formed during the first round of the HCl gas etching process, as evidenced by the shapes of the SiO_2 sidewall masks.

In this study, we proposed a crystallographic undercutting etching method for (100) β-Ga_2O_3, and we demonstrated its efficacy in obtaining air bridges. The key process step was crystallographic gas etching, which enabled horizontal etching to progress along the (100) plane, which has the lowest surface energy density. We believe that our simple air-gap manufacturing process, which requires no peeling, transferring, or bonding, will be readily welcomed, particularly in the field of β-Ga_2O_3-based MEMS.

ACKNOWLEDGMENTS

This work was supported by the Nanofabrication and Electron Microscopy Units in the National Institute for Materials Science and the Advanced Research Infrastructure for Materials and Nanotechnology in Japan of the Ministry of Education, Culture, Sports, Science, and Technology (Grant No. JPMXP1224NM5062). This work was financially supported by the TEPCO Memorial Foundation and Grant-in-Aid for Scientific Research (B) of the Japan Society for the Promotion of Science under Grant No. JP24K01368.

AUTHOR DECLARATIONS

Conflict of Interest

The authors have no conflicts to disclose.

Author Contributions

Takayoshi Oshima: Conceptualization (equal); Methodology (equal); Writing – original draft (lead); Writing – review & editing (equal). **Yuichi Oshima**: Methodology (equal); Writing – review & editing (equal).

DATA AVAILABILITY

The data that support the findings of this study are available from the corresponding author upon reasonable request.

REFERENCES

[1] T. Onuma, S. Saito, K. Sasaki, T. Masui, T. Yamaguchi, T. Honda, and M. Higashiwaki, Jpn. J. Appl. Phys. **54**, 112601 (2015).
[2] M. Higashiwaki, K. Sasaki, A. Kuramata, T. Masui, and S. Yamakoshi, Appl. Phys. Lett. **100**, 013504 (2012).
[3] T. Oshima, T. Okuno, N. Arai, N. Suzuki, S. Ohira, and S. Fujita, Appl. Phys. Express **1**, 011202 (2008).
[4] T. Oshima, T. Okuno, N. Arai, N. Suzuki, H. Hino, and S. Fujita, Jpn. J. Appl. Phys. **48**, 011605 (2009).
[5] S. Jang, S. Jung, J. Kim, F. Ren, S. J. Pearton, and K. H. Baik, ECS J. Solid State Sci. Technol. **7**, Q3180–Q3182 (2018).
[6] M. Bartic, Y. Toyoda, C.-I. Baban, and M. Ogita, Jpn. J. Appl. Phys. **45**, 5186 (2006).
[7] E. G. Víllora, K. Shimamura, Y. Yoshikawa, K. Aoki, and N. Ichinose, J. Cryst. Growth **270**, 420–426 (2004).
[8] A. Kuramata, K. Koshi, S. Watanabe, Y. Yamaoka, T. Masui, and S. Yamakoshi, Jpn. J. Appl. Phys. **55**, 1202A2 (2016).
[9] Z. Galazka, R. Uecker, D. Klimm, K. Irmscher, M. Naumann, M. Pietsch, A. Kwasniewski, R. Bertram, S. Ganschow, and M. Bickermann, ECS J. Solid State Sci. Technol. **6**, Q3007–Q3011 (2017).
[10] Y. Ueda, T. Igarashi, K. Koshi, S. Yamakoshi, K. Sasaki, and A. Kuramata, Jpn. J. Appl. Phys. **62**, SF1006 (2023).
[11] A. Yoshikawa, V. Kochurikhin, T. Tomida, I. Takahashi, K. Kamada, Y. Shoji, and K. Kakimoto, Sci. Rep. **14**, 14881 (2024).
[12] K. Sasaki, Appl. Phys. Express **17**, 090101 (2024).
[13] X.-Q. Zheng, H. Zhao, and P. X. L. Feng, Appl. Phys. Lett. **120**, 040502 (2022).
[14] M.-F. Yu, M. Z. Atashbar, and X. Chen, IEEE Sens. J. **5**, 20–25 (2005).
[15] X.-Q. Zheng, J. Lee, S. Rafique, L. Han, C. A. Zorman, H. Zhao, and P. X. L. Feng, ACS Appl. Mater. Interfaces **9**, 43090–43097 (2017).
[16] X.-Q. Zheng, H. Zhao, Z. Jia, X. Tao, and P. X. L. Feng, Appl. Phys. Lett. **119**, 013505 (2021).
[17] X.-Q. Zheng, T. Kaisar, and P. X.-L. Feng, Appl. Phys. Lett. **117**, 243504 (2020).
[18] X.-Q. Zheng, J. Lee, S. Rafique, M. R. Karim, L. Han, H. Zhao, C. A. Zorman, and P. X. L. Feng, IEEE Electron Device Lett. **39**, 1230–1233 (2018).
[19] X.-Q. Zheng, Y. Xie, J. Lee, Z. Jia, X. Tao, and P. X. L. Feng, APL Mater. **7**, 022523 (2019).
[20] W. Sui, S. M. Enamul Hoque Yousuf, Y. Liu, S. J. Pearton, and P. X. L. Feng, Adv. Mater. Technol. **9**, 2301356 (2024).
[21] T. Oshima, T. Okuno, N. Arai, Y. Kobayashi, and S. Fujita, Jpn. J. Appl. Phys. **48**, 040208 (2009).

[22]Y. Zhang, A. Mauze, and J. S. Speck, Appl. Phys. Lett. **115**, 013501 (2019).
[23]S. Rebollo, T. Itoh, S. Krishnamoorthy, and J. S. Speck, Appl. Phys. Lett. **125**, 012102 (2024).
[24]S. Jang, S. Jung, K. Beers, J. Yang, F. Ren, A. Kuramata, S. J. Pearton, and K. H. Baik, J. Alloys Compd. **731**, 118–125 (2018).
[25]Y. Kim, J. Baek, K. H. Baik, and S. Jang, Appl. Surf. Sci. **665**, 160330 (2024).
[26]T. Oshima and Y. Oshima, Appl. Phys. Lett. **122**, 162102 (2023).
[27]Y. Oshima and T. Oshima, Jpn. J. Appl. Phys. **62**, 080901 (2023).
[28]T. Oshima and Y. Oshima, Appl. Phys. Express **16**, 066501 (2023).
[29]T. Oshima and Y. Oshima, Appl. Phys. Lett. **124**, 042110 (2024).
[30]T. Oshima and Y. Oshima, Jpn. J. Appl. Phys. **64**, 018003 (2025).
[31]T. Oshima, R. Togashi, and Y. Oshima, Sci. Technol. Adv. Mater. **25**, 2378683 (2024).
[32]Y. Ooe, Y. Kawasaki, Y. Moriya, D. Ito, and A. Kikuchi, "Hydrogen environment anisotropic thermal etching of (010) β-Ga_2O_3 and fabrication of high-aspect Ga_2O_3 nanowall structures," in 3rd 4th International Workshop Gallium Oxide Related Materials (2019).
[33]Y. Yamazaki, M. Tomoaki, A. Takeki, and A. Kikuchi, "Fabrication of high aspect DBR structures for optical integrated devices by hydrogen environment anisotropic thermal etching of β-Ga_2O_3," in 4th International Workshop Gallium Oxide Related Materials (2022).
[34]S. Sato, T. Momma, T. Aikawa, and A. Kikuchi, "Fabrication of mesa-shaped high-aspect Ga_2O_3/Air DBR structures for optical integrated platform by HEATE method," in 5th International Workshop Gallium Oxide Related Materials (2024).
[35]S. Mu, M. Wang, H. Peelaers, and C. G. Van de Walle, APL Mater. **8**, 091105 (2020).
[36]N. K. Kalarickal, A. Fiedler, S. Dhara, H.-L. Huang, A. F. M. A. U. Bhuiyan, M. W. Rahman, T. Kim, Z. Xia, Z. J. Eddine, A. Dheenan, M. Brenner, H. Zhao, J. Hwang, and S. Rajan, Appl. Phys. Lett. **119**, 123503 (2021).
[37]S. Dhara, N. K. Kalarickal, A. Dheenan, S. I. Rahman, C. Joishi, and S. Rajan, Appl. Phys. Lett. **123**, 023503 (2023).
[38]A. Katta, F. Alema, W. Brand, A. Gilankar, A. Osinsky, and N. K. Kalarickal, J. Appl. Phys. **135**, 075705 (2024).
[39]N. Das, F. Alema, W. Brand, A. Katta, A. Gilankar, A. Osinsky, and N. K. Kalarickal, arXiv:2408.05824 (2024).
[40]R. Schewski, M. Baldini, K. Irmscher, A. Fiedler, T. Markurt, B. Neuschulz, T. Remmele, T. Schulz, G. Wagner, Z. Galazka, and M. Albrecht, J. Appl. Phys. **120**, 225308 (2016).
[41]R. Schewski, K. Lion, A. Fiedler, C. Wouters, A. Popp, S. V. Levchenko, T. Schulz, M. Schmidbauer, S. Bin Anooz, R. Grüneberg, Z. Galazka, G. Wagner, K. Irmscher, M. Scheffler, C. Draxl, and M. Albrecht, APL Mater. **7**, 022515 (2019).
[42]K. Tetzner, E. Bahat Treidel, O. Hilt, A. Popp, S. Bin Anooz, G. Wagner, A. Thies, K. Ickert, H. Gargouri, and J. Wurfl, IEEE Electron Device Lett. **40**, 1503–1506 (2019).
[43]K. Tetzner, M. Klupsch, A. Popp, S. Bin Anooz, T.-S. Chou, Z. Galazka, K. Ickert, M. Matalla, R.-S. Unger, E. B. Treidel, M. Wolf, A. Trampert, J. Würfl, and O. Hilt, Jpn. J. Appl. Phys. **62**, SF1010 (2023).
[44]S. Geller, J. Chem. Phys. **33**, 676–684 (1960).